Technical University of Denmark

DTU

Coherent supercontinuum bandwidth limitations under femtosecond pumping at 2 μm in all-solid soft glass photonic crystal fibers

Klimczak, Mariusz; Siwicki, Bartomiej; Zhou, Binbin; Bache, Morten; Pysz, Dariusz; Bang, Ole; Buczyski, Ryszard

DTU Library
Technical Information Center of Denmark

Coherent supercontinuum bandwidth limitations under femtosecond pumping at 2 µm in all-solid soft glass photonic crystal fibers

MARIUSZ KLIMCZAK,[1,*] BARTŁOMIEJ SIWICKI,[1,2] BINBIN ZHOU,[3] MORTEN BACHE,[3] DARIUSZ PYSZ,[1] OLE BANG,[3] AND RYSZARD BUCZYŃSKI[1,2]

[1]*Glass Department, Institute of Electronic Materials Technology, Wolczynska 133, 01-919 Warsaw, Poland*
[2]*Faculty of Physics, University of Warsaw, Pasteura 7, 02-093 Warsaw, Poland*
[3]*DTU Fotonik, Department of Photonics Engineering, Technical University of Denmark, DK-2800 Kgs. Lyngby, Denmark*
[*]*mariusz.klimczak@itme.edu.pl*

Abstract: Two all-solid glass photonic crystal fibers with all-normal dispersion profiles are evaluated for coherent supercontinuum generation under pumping in the 2.0 µm range. In-house boron-silicate and commercial lead-silicate glasses were used to fabricate fibers optimized for either flat dispersion, albeit with lower nonlinearity, or with larger dispersion profile curvature but with much higher nonlinearity. Recorded spectra at the redshifted edge reached 2500-2800 nm depending on fiber type. Possible factors behind these differences are discussed with numerical simulations. The fiber enabling the broadest spectrum is suggested as an efficient first stage of an all-normal dispersion cascade for coherent supercontinuum generation exceeding 3000 nm.

References and links

1. U. Sharma, E. W. Chang, and S. H. Yun, "Long-wavelength optical coherence tomography at 1.7 µm for enhanced imaging depth," Opt. Express **16**(24), 19712–19723 (2008).
2. C. S. Colley, J. C. Hebden, D. T. Delpy, A. D. Cambrey, R. A. Brown, E. A. Zibik, W. H. Ng, L. R. Wilson, and J. W. Cockburn, "Mid-infrared optical coherence tomography," Rev. Sci. Instrum. **78**(12), 123108 (2007).
3. H. Kawagoe, S. Ishida, M. Aramaki, Y. Sakakibara, E. Omoda, H. Kataura, and N. Nishizawa, "Development of a high power supercontinuum source in the 1.7 µm wavelength region for highly penetrative ultrahigh-resolution optical coherence tomography," Biomed. Opt. Express **5**(3), 932–943 (2014).
4. C. S. Cheung, J. M. O. Daniel, M. Tokurakawa, W. A. Clarkson, and H. Liang, "High resolution Fourier domain optical coherence tomography in the 2 µm wavelength range using a broadband supercontinuum source," Opt. Express **23**(3), 1992–2001 (2015).
5. Y. Takushima and K. Kikuchi, "10-GHz Over 20-Channel multiwavelength pulse source by slicing super-continuum spectrum generated in normal-dispersion fiber," IEEE Photonics Technol. Lett. **11**(3), 322–324 (1999).
6. C.-B. Huang, S.-G. Park, D. E. Leaird, and A. M. Weiner, "Nonlinearly broadened phase-modulated continuous-wave laser frequency combs characterized using DPSK decoding," Opt. Express **16**(4), 2520–2527 (2008).
7. R. Wu, V. Torres-Company, D. E. Leaird, and A. M. Weiner, "Supercontinuum-based 10-GHz flat-topped optical frequency comb generation," Opt. Express **21**(5), 6045–6052 (2013).
8. Z. Liu, Y. Chen, Z. Li, B. Kelly, R. Phelan, J. O'Carroll, T. Bradley, J. P. Wooler, N. V. Wheeler, A. M. Heidt, T. Richter, C. Schubert, M. Becker, F. Poletti, M. N. Petrovich, S. Alam, D. J. Richardson, and R. Slavík, "High-capacity directly modulated optical transmitter for 2-µm spectral region," J. Lightwave Technol. **33**(7), 1373–1379 (2015).
9. A. M. Heidt, A. Hartung, G. W. Bosman, P. Krok, E. G. Rohwer, H. Schwoerer, and H. Bartelt, "Coherent octave spanning near-infrared and visible supercontinuum generation in all-normal dispersion photonic crystal fibers," Opt. Express **19**(4), 3775–3787 (2011).
10. A. M. Heidt, "Pulse preserving flat-top supercontinuum generation in all-normal dispersion photonic crystal fibers," J. Opt. Soc. Am. B **27**(3), 550–559 (2010).

11. W. J. Tomlinson, R. H. Stolen, and A. M. Johnson, "Optical wave breaking of pulses in nonlinear optical fibers," Opt. Lett. **10**(9), 457–459 (1985).
12. G. P. Agrawal, *Nonlinear Fiber Optics* (Academic, 2001).
13. A. M. Heidt, J. Rothhardt, A. Hartung, H. Bartelt, E. G. Rohwer, J. Limpert, and A. Tünnermann, "High quality sub-two cycle pulses from compression of supercontinuum generated in all-normal dispersion photonic crystal fiber," Opt. Express **19**(15), 13873–13879 (2011).
14. N. Nishizawa and J. Takayanagi, "Octave spanning high-quality supercontinuum generation in all-fiber system," J. Opt. Soc. Am. B **24**(8), 1786–1792 (2007).
15. M. Klimczak, B. Siwicki, P. Skibiński, D. Pysz, R. Stępień, A. Heidt, C. Radzewicz, and R. Buczyński, "Coherent supercontinuum generation up to 2.3 µm in all-solid soft-glass photonic crystal fibers with flat all-normal dispersion," Opt. Express **22**(15), 18824–18832 (2014).
16. X. Feng, T. Monro, P. Petropoulos, V. Finazzi, and D. Hewak, "Solid microstructured optical fiber," Opt. Express **11**(18), 2225–2230 (2003).
17. T. Martynkien, D. Pysz, R. Stępień, and R. Buczyński, "All-solid microstructured fiber with flat normal chromatic dispersion," Opt. Lett. **39**(8), 2342–2345 (2014).
18. X. Li, W. Chen, T. Xue, J. Gao, W. Gao, L. Hu, and M. Liao, "Low threshold mid-infrared supercontinuum generation in short fluoride-chalcogenide multimaterial fibers," Opt. Express **22**(20), 24179–24191 (2014).
19. S. Kedenburg, T. Steinle, F. Mörz, A. Steinmann, and H. Giessen, "High-power mid-infrared high repetition-rate supercontinuum source based on a chalcogenide step-index fiber," Opt. Lett. **40**(11), 2668–2671 (2015).
20. D. Lorenc, M. Aranyosiova, R. Buczynski, I. Stepien, I. Bugar, A. Vincze, and D. Velic, "Nonlinear refractive index of multicomponent glasses designed for fabrication of photonic crystal fibers," Appl. Phys. B **93**(2–3), 531–538 (2008).
21. V. L. Kalashnikov, E. Sorokin, and I. T. Sorokina, "Raman effects in the infrared supercontinuum generation in soft-glass PCFs," Appl. Phys. B **87**(1), 37–44 (2007).
22. J. C. Travers, M. H. Frosz, and J. M. Dudley, "Nonlinear fiber optics overview," in *Supercontinuum Generation in Optical Fibers*, J. M. Dudley, R. Taylor, ed. (Cambridge University 2010), pp. 32–51.
23. B. Kibler, J. M. Dudley, and S. Coen, "Supercontinuum generation and nonlinear pulse propagation in photonic crystal fiber: influence of the frequency-dependent effective mode area," Appl. Phys. B **81**(2-3), 337–342 (2005).
24. L. Liu, T. Cheng, K. Nagasaka, H. Tong, G. Qin, T. Suzuki, and Y. Ohishi, "Coherent mid-infrared supercontinuum generation in all-solid chalcogenide microstructured fibers with all-normal dispersion," Opt. Lett. **41**(2), 392–395 (2016).
25. C. R. Petersen, P. M. Moselund, C. Petersen, U. Møller, and O. Bang, "Spectral-temporal composition matters when cascading supercontinua into the mid-infrared," Opt. Express **24**(2), 749–758 (2016).

1. Introduction

Applications like optical coherence tomography (OCT) or generation of stable frequency combs can greatly benefit from spatially coherent and ultra-stable supercontinuum (SC) light sources with long-range near-infrared (NIR) wavelengths (1.5-3.0 µm). In OCT it is advantageous to change the probe light from 1.3 µm into longer wavelengths to increase penetration depth by avoiding water absorption [1] or by covering the fingerprint region and enabling contrast agent-free imaging [2]. It is also advantageous to use an SC based on all-normal dispersion (ANDi) fibers, because of their high coherence and smooth spectra. Specifically, using such an ANDi SC, the change of OCT operation wavelength enabled a 10 dB increase of signal-to-noise (SNR) ratio [3]. A similar advantage was recently reported for OCT imaging of non-biological samples using probe light in the 2.0 µm range [4], where a 10 dB SNR improvement was observed when an amplified spontaneous emission (ASE) source was replaced with an SC laser. Excellent noise performance is of paramount importance in various frequency conversion applications and for novel telecommunication devices. Frequency comb generation, pumped with laser diode driven ANDi SC was demonstrated, covering a 10 GHz bandwidth with 20 channels around 1558 nm, with 6.8 dB flatness [5]. More recently, it was shown that ANDi SC pumping against anomalous-dispersion pumping enabled a major improvement of the bit-error-rate in phase-shift keying transmission [6]. Significant enhancement of the number of channels and bandwidth up to 365 lines over 3.64 THz in the C-band, with 3.5 dB flatness, was also demonstrated in an ANDi SC-pumped comb [7]. It can be expected, that comb-based sources would also benefit from a redshift of the operation wavelength into the 2 µm area, which is becoming the emerging direction of development of the next-generation, ultra-low loss and low latency telecommunications band [8].

ANDi SC is well-known for its excellent coherence properties compared to anomalous dispersion pumped SC [9,10]. Under femtosecond pulse pumping, the development of spectrum is facilitated by self-phase modulation (SPM), followed by optical wave breaking (OWB [11],). Both processes are self-seeded and noise amplification is absent. Although this in particular is true also for anomalous-dispersion pumped soliton-based SC sources (provided that ultrashort pulses are used so the SC spectrum develops over a propagation distance shorter than the modulation instability length-scale [12]), the advantage of an ANDi SC over a soliton-based SC is a uniform temporal profile of the SC pulse. This enables recompression close to the single-cycle limit using phase-compensation methods [13]. ANDi SC pumped at around 1.55 µm and extending past 2.0 µm with their redshifted side-band have already been reported [14,15]. The all-solid glass approach to photonic crystal fiber (PCF) fabrication [16] allows broadband flattening of the ANDi profile, as shown in oxide soft glass fibers [15,17]. A hybrid ZBLAN-chalcogenide ANDi PCF was also demonstrated to generate an SC spectrum spanning 1.2-2.7 µm under pumping around 1.9 µm with 100 fs pulses [18], where ZBLAN is the well-known ZrF_4-BaF_2-LaF_3-AlF_3-NaF heavy-metal fluoride glass composition. Unfortunately, the reported spectrum had an excessive dip around the pump wavelength, which would require further optimization of the dispersion profile, as suggested earlier [10]. It is to be noted that selected, commercially available chalcogenide glass step-index fibers do enable coherent ANDi SC generation, as reported in [19], where a spectrum spanning 2-5 µm was demonstrated, albeit a non-standard pump wavelength of 3.83 µm was required in that specific case.

In this work we demonstrate a new all-solid glass photonic crystal fiber with all-normal, flattened dispersion profile. This fiber is confronted in context of ANDi supercontinuum generation with the design reported earlier [15,17]. Both fiber types were made from silicate soft glasses and specifically the photonic lattice of the new ANDi PCF was composed of two commercially available glasses F2 and SF6 (Schott). The fibers are pumped at 2160 nm from an OPA system delivering 60 fs pulses, with the specific wavelength chosen to be in the middle of the flat ANDi landscape. In such pumping conditions, ANDi SC generation performance of the fibers was evaluated closely to their long-wavelength transmission cutoff, as well as in the spectral range generally accessible with the emerging, high average power femtosecond thulium-doped lasers. The obtained experimental results are discussed in the context of possible limitations of the spectral width of the SC, related to the fiber's attenuation, nonlinearity and dispersion parameters.

2. Fibers and methods

Two types of all-solid glass photonic crystal fibers are considered. Their scanning electron microscopy images are shown in Fig. 1 and the geometrical parameters are summarized in Table 1. Both fibers have a hexagonal lattice layout, in which the air-holes of the photonic cladding were replaced with another glass, thermally matched to the glass in the lattice and the core. The original design of fibers, reported previously and in this work labeled NL21C2 and NL21C4, consisted of a lattice and core made from F2 glass from Schott, with the lattice holes filled with inclusions made from in-house boron-silicate glass [15,17]. The refractive indices of the F2 and the boron-silicate glass, measured at 1550 nm, are 1.5948 (core and lattice glass) and 1.5113 (lattice inclusions). This PCF type hence supports index guiding. Based on this design, the second series of fibers was developed – labeled NL38A2 and NL38A4. In this type, the lattice glass was replaced with Schott's SF6 and F2 was used for the glass lattice inclusions. Near-infrared transmission spectra measured in bulk SF6 and F2 glass samples are shown in Fig. 2 (Fresnel reflections compensated for by subtracting results obtained in 5 mm and 10 mm thick samples). Both glasses used for the core of NL21 and NL38 series PCFs, respectively, have very similar transmission characteristics with the long-wavelength absorption edge located at about 2750 nm. There is a 1-2 percentage point difference between the two glasses at wavelengths over 2000 nm. The refractive index of the

SF6 glass at 1550 nm is 1.7641. The refractive index contrast in the NL38 type fibers is therefore 0.2528, which is significantly higher than for the NL21 type (0.0871). Consequently, the wavelength dependence of the effective mode area of the latter fiber type (NL38) is smaller than for the NL21 type fibers, as shown in Fig. 3(a). According to simulations, the cutoff wavelength for the higher-order modes in the NL21 fibers is around 1300 nm, while for the NL38 type it is at about 1600 nm. The dispersion profiles of both fiber types are shown in Fig. 3(b). The tighter mode confinement of the NL38 fibers is here seen to come at the cost of a more sloped dispersion profile, compared to the spectrally broad, flattened saddle of the dispersion of the NL21 type fibers. As can be seen in particular for the NL38 PCFs, there has been a slight deviation of the measured dispersion profile from the calculated characteristics. This is assigned to the diffusion taking place during fiber drawing at the interfaces of the two glasses forming the lattice, which is very difficult to account for in numerical modelling. Calculated confinement loss for the fundamental mode of the two fiber geometries are shown in Fig. 3(c). In both cases the loss level of the waveguide itself (neglecting material loss) is negligible within the wavelength range of interest. We extended the simulations based on theoretical material dispersion profiles of the fiber glasses and note, that the loss level of the fundamental mode for any of the considered PCF geometries would become noticeable only at wavelengths far outside of their transmission window. From our experience with these fibers, we note that they are insensitive to bending in terms of loss and their birefringence is negligible. The values of the nonlinear refractive index for the three glasses are: NC21A $n_2 = 1.1 \times 10^{-20}$ m^2/W and F2 $n_2 = 2.9 \times 10^{-20}$ m^2/W (both measured at 1240 nm [19]) and SF6 $n_2 = 21 \times 10^{-20}$ m^2/W (reported for 1500 nm [21]). In the SC generation simulations discussed later, n_2 values of the F2 and SF6 core glasses were used for the NL21 and NL38 fiber types, respectively.
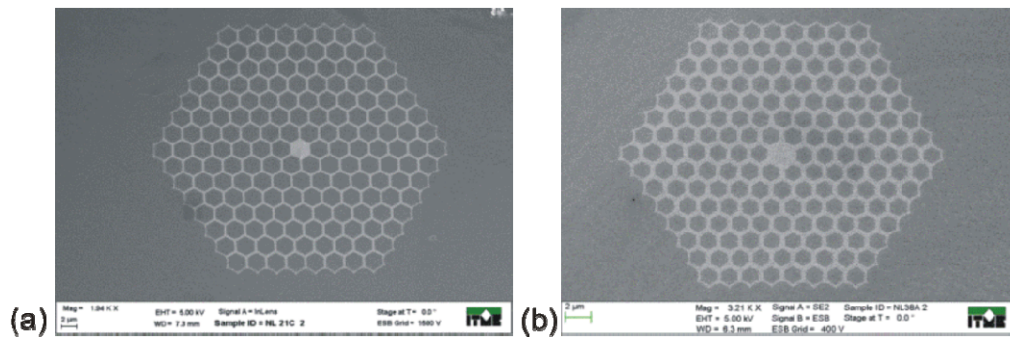

Fig. 1. Scanning electron microscopy images of the end facets of a) NL21 series: core and lattice (light color) are made of F2 glass and lattice inclusions and surrounding tube are from NC21A glass, b) NL38 series: SF6 in the core and lattice, F2 in the inclusions and the surrounding tube.
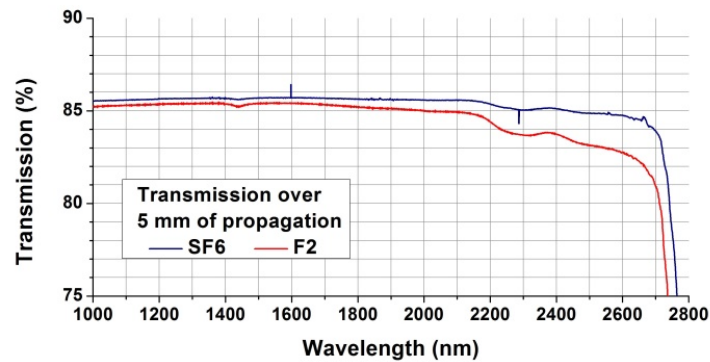
Fig. 2. Transmission spectra of bulk SF6 and F2 glass samples measured over 5 mm of propagation.

Table 1. Geometrical parameters of NL21C and NL38A fibers.

Fiber	NL21C2	NL21C4	NL38A2	NL38A4
Inclusion size [μm]	2.3	2.2	1.25	1.2
Lattice constant [μm]	2.56	2.41	1.55	1.54
Core diameter* [μm]	2.46	2.46	2.27	2.21
Lattice diameter [μm]	38.0	35.6	25.3	24.6
Outer diameter [μm]	155	143	120	117

*Defined as the diameter of the circle inscribed by the inner ring of hexagons.
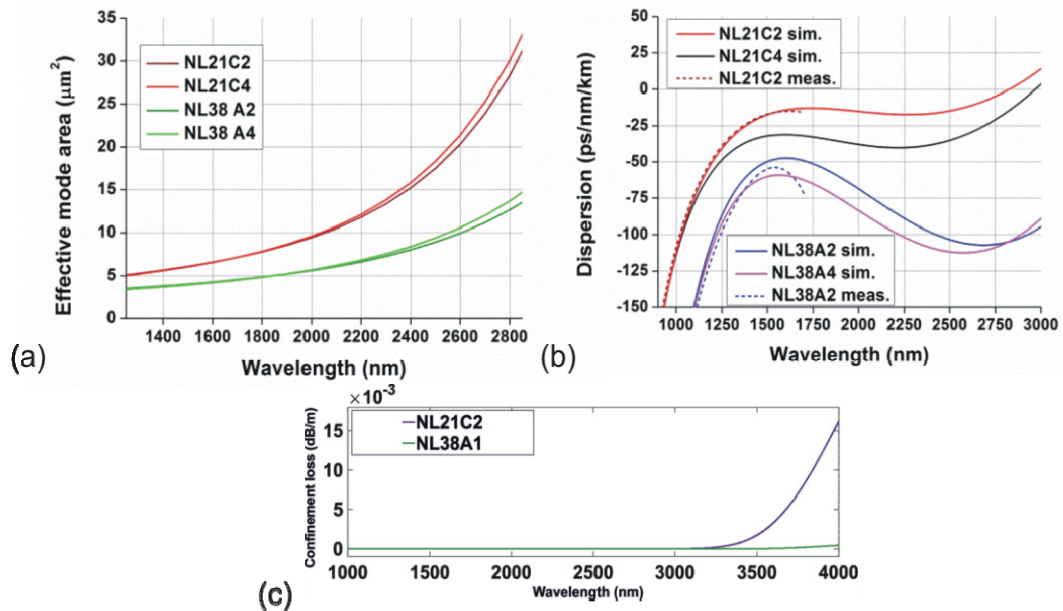

Fig. 3. (a) Calculated effective mode areas of the PCFs, (b) theoretical (solid traces) and measured (dotted traces) dispersion profiles of the considered PCFs, (c) confinement loss calculated for both PCF geometries (material loss neglected).

The pump source used in all experiments was an Optical Parametric Amplifier (OPA) with 1 kHz repetition rate. It delivered 60 fs Gaussian-shaped pulses (135 nm spectral with, 50 fs transform-limited duration), and was tuned to 2160 nm. We intended to pump the fibers close to the multi-phonon cutoff of their transmission window (about 2800 nm) and yet stay roughly in the middle of the flattened dispersion "saddle" point of one of the fibers (as shown

later). The detection system in the experimental setup consisted of an InGaAs CCD spectrometer with 900-2500 nm wavelength coverage. Spectra extending to wavelengths longer than 2500 nm were recorded with a mid-IR diffraction grating monochromator equipped with a liquid-nitrogen cooled MCT detector and a box-car integrator.

3. Experimental results

The normal dispersion profile of the NL21 series PCFs is flat around the selected pump wavelength of 2160 nm to within about 10 ps/nm/km. It stretches towards the redshifted and blue-shifted wavelengths for roughly ± 650 nm. Figure 4 shows the measured SC spectra in 30 cm long samples of these fibers, under pumping at 2160 nm with 60 fs pulses. Average pump powers shown for reference next to the respective spectra in Fig. 4, and later in Fig. 5, were measured before the coupling lens and included closely propagating signal, idler and residual pump beams. The actual pump power incident on the fiber facet was coming from the 2160 nm idler and was much smaller, due to small aperture of the coupling lens, which was anti-reflection coated for 1.8-3.0 μm. All spectra are somewhat asymmetric in the wavelength scale and the broadening is taking place practically only at the blue-shifted wavelengths. The long-wavelength edge of the SC, confirmed using the mid-IR monochromator, was located at a wavelength shorter than 2500 nm and it is in principle the pump spectrum, also shown in Fig. 4. The short-wavelength edge reaches almost 900 nm in a 20 dB dynamic range for the case of the widest spectrum. Comparing the two fibers, it can be noticed that the NL21C2 fiber outperforms the NL21C4 in terms of the reach of spectrum towards the blue-shifted wavelengths by roughly 250 nm. The spectra in both fibers are flat to about 5 dB for at least an octave.

The SC spectra recorded in the second family of fibers, the NL38, are shown in Fig. 5. The fiber sample length was again 30 cm. The broadest spectrum extends to about 1150 nm at the blue-shifted edge. At the redshifted edge, all spectra cut off at about 2750 nm due to the limit of the glass transmission. This series of PCFs was more resistant to pump laser damage than the NL21 fibers, and thus was pumped stronger. We note that similar spectra to those shown in Fig. 5 were obtainable already at pump powers comparable to what was used with NL21 series. The result shown in Fig. 5 were the broadest spectra obtained with these fibers at pump powers still below their damage threshold. The spectra in the NL38 fibers are not as flat as in the NL21 type, which is related to the stronger slopes at the "saddle" of the dispersion profile of NL38 fibers, Fig. 3(b). Sloped dispersion is in general disadvantageous for ANDi SC generation, because it means introducing larger relative delays of the adjacent spectral components during broadening [10]. Various delays introduced across the spectra in the NL38 fibers result in less spectral flatness, compared with the spectra in NL21 fibers. Especially for the NL38A2 fiber and the higher pump power, there is a prominent peak in the SC around 1500 nm - Fig. 5(a) - which can be related to the broad peak of the dispersion profile of the fiber, which has a maximum at about 1300 nm, Fig. 3(b). The dispersion profiles of NL38 fibers are less flat than in the NL21 fibers. Yet, the SC spectra recorded in the NL38 fibers extend up to the glass transmission cutoff at about 2800 nm, while spectra in NL21 fibers are limited to 2500 nm.
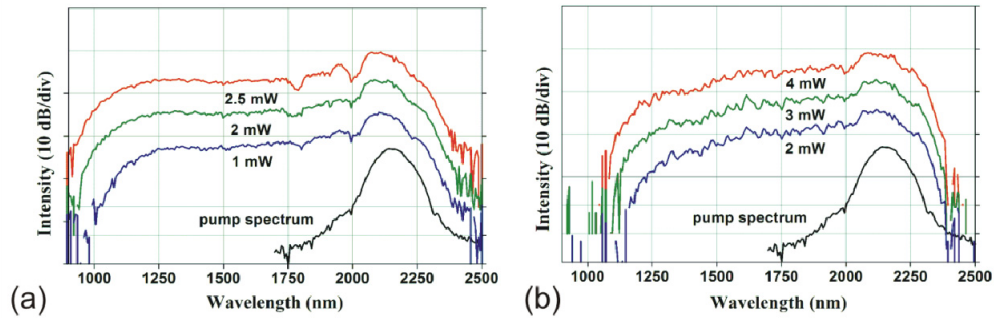
Fig. 4. Supercontinuum spectra measured in the NL21 series PCFs: (a) NL21C2 fiber, (b) NL21C4 fiber. The pump source was an OPA operating at 2160 nm, pulse length was 60 fs.
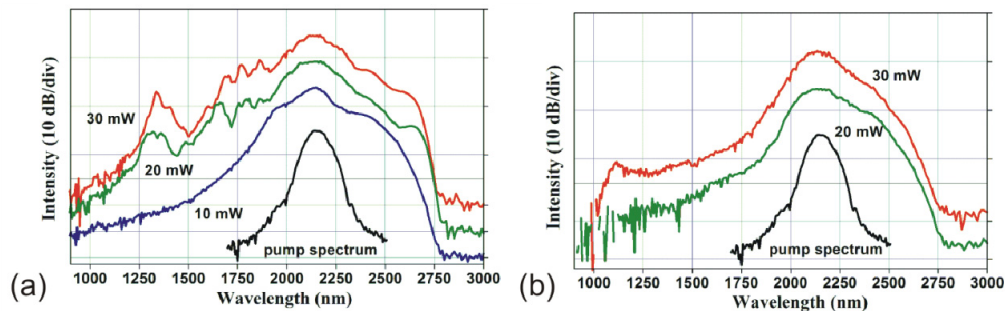

Fig. 5. Supercontinuum spectra measured in the NL38 series PCFs: (a) NL38A2, (b) NL38A4. The pump source was an OPA operating at 2160 nm, pulse length was 60 fs.

The values of the linear refractive indices of the glasses in all-solid glass PCFs can also be of importance in this context. The refractive index contrast between the core and the cladding in such a fiber is smaller than in a corresponding air-glass fiber structure with similar air-filling factor (similar to the relative inclusion size of the all-solid structured fiber). An all-solid glass PCF will typically have weaker mode confinement than an air-glass lattice fiber with comparable core diameter, or another all-solid glass PCF made from glasses with higher refractive index contrast. The latter is shown in Fig. 3(a) with the wavelength dependence profiles of the effective mode areas numerically calculated for the NL21 and NL38 type fibers. The effective mode areas at the long-wavelength edge of the transmission window of the fibers (around 2800 nm) are about 30 μm^2 and 12 μm^2 respectively, for the two fiber types. NL21 series fibers have a roughly 12 μm^2 effective mode area already at about 2400 nm, which rapidly increases at longer wavelengths.

A large difference of the linear refractive index in an air-hole PCF structure is desirable for tight mode confinement in a wide range of wavelengths. Introduction of another glass into this structure works against this but is advantageous to the flexibility of the dispersion profile engineering [17]. The two presented all-solid glass PCFs demonstrate this dilemma with the NL21 fiber (smaller refractive index difference) enabling a flatter saddle of the dispersion profile and a flatter SC spectrum, while the NL38 fiber (larger refractive index difference) allows better mode confinement with more spectrum towards the redshifted wavelengths.

4. Nonlinear simulations of ANDi SC

Figure 6 contains results of full dynamical simulations, in which these two alternatives are reconstructed numerically. Modeling is referenced to experimental results obtained for the broader SC spectra obtained in each of the fiber types: NL21C2 - Fig. 6(a) - and NL38A2, Fig. 6(b). In each case, the spectrum is modeled using the generalized nonlinear Schrödinger equation (GNSLE). The code proposed by Travers et al. was used [22], because of its clarity

and ease of extension. Specifically, we extended the model with the frequency dependence of the affective mode area $A_{eff}(\omega)$ and frequency-dependent loss $\alpha(\omega)$ – both parameters are referred to by their dependence on the wavelength in the later part of work. Additionally, simulations with effective mode area fixed to the value at the used pump wavelength (see Table 2) were performed and included in Fig. 6 for both fiber geometries. The loss was modeled with Lorentzian line-shapes centered at 1380 nm and 1850 nm with full width at half-maximum of about 50 nm and 100 nm, respectively, representing the OH‾ impurity bands (peaking at 6 dB and 3 dB above the background loss, respectively). Calculated confinement loss - Fig. 2 - was neglected and the same model of loss characteristic was assumed for all fibers, for simplicity. The actual attenuation spectrum included in all simulations is shown in Fig. 7. Fiber length assumed in all simulations was 30 cm, as in the physical measurements. The transmission cutoff, modeled with a steep exponential edge, is located at about 2800 nm in all simulations. Apart from these wavelength-dependent features, a 2 dB/m flat loss base was also used. Simulations assuming fixed A_{eff} values and a lossless fiber (no transmission edge, no OH‾ nor background losses) were also performed and are shown in Fig. 7. The modeling included Raman scattering, although it can be safely assumed, that it would be strongly suppressed by SPM and OWB under pumping with 60 fs long pulses [9,10]. The pulse energy assumed in all simulations was 1 nJ. This assumption includes the fact, that this was the energy actually contained in the core area of fiber, which experiences nonlinearity and contributes to formation of the supercontinuum. We note, that in reality, part of the pulse couples into the lattice, where it can propagate as well, but without spectral broadening; this can explain most of the experimentally observed peak around the pump wavelength that is not reproduced by the simulations. All numerical spectra were recalculated for power spectral density, before comparing with experimental results.

Results of numerical simulations with wavelength-dependent effective mode area for the NL21C2 fiber, Fig. 6(a), are in a reasonable agreement with the experimental result. Some differences in spectral intensity observable around the pump wavelength are assigned to part of the pump power propagating in the photonic lattice, as reported earlier for this type of PCF [15]. The larger intensity at the blue-shifted edge of spectrum, recorded experimentally, is assigned to excitation of higher-order modes, which are guided at these wavelengths [15]. The simulation shows that the obtainable spectral width in this type of fiber is about an octave in the 1000-2300 nm area, regardless of pumping at 1560 nm [15] or pumping at 2160 nm shown here. Comparing the earlier result reported in [15], it is to be noted, that the blue-shifted edge of SC extends towards about 900-1000 nm, regardless of the pump wavelength used (while its peak power remains comparable). Simulation results for this fiber variant with the effective mode area fixed to the value of 11.5 μm^2 (at 2160 nm) reveals that a significant part of the blue-shifted wing of spectrum is missing. This is a consequence of a large difference of A_{eff} value in both simulations (fixed and λ-dependent A_{eff} scenario) at wavelengths shorter than the pump wavelength. On the contrary, the redshifted broadening is practically unchanged. The increased nonlinearity stemming from a fixed value of A_{eff} does not improve the redshifted spectrum's width, despite the favorable flat ANDi dispersion characteristic in these fibers, Fig. 3(b). Only in a lossless fiber scenario does the NL21 series PCF produce more redshifted bandwidth. We note that this should not lead to a conclusion, that fiber attenuation is the main limiting mechanism in this case, since for the NL38 fibers, where exactly the same loss model was assumed, the spectrum readily extends towards the red. It must be concluded, that it is the low nonlinearity of the fiber (even neglecting the A_{eff}-related decrease of nonlinearity at increasing wavelengths), which in presence of the inherent fiber background loss, precludes redshifted broadening.
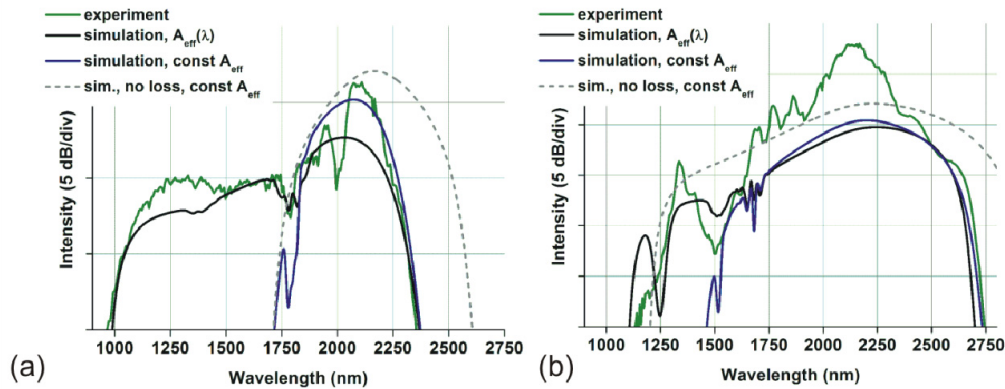
Fig. 6. Reconstruction of experimental spectra with numerical simulations: (a) NL21C2 fiber, (b) NL38A2 fiber.
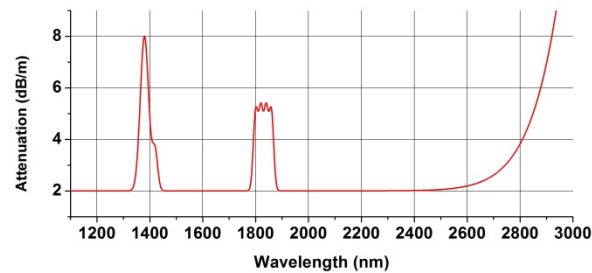

Fig. 7. Modelled attenuation spectrum assumed in all simulations.

Further improvement of PCF nonlinearity is however possible in a physical situation, when the second PCF type is considered. Obtained experimental results for the NL38A2 fiber are confronted with simulations in Fig. 6(b). The higher refractive index contrast of the glasses used for NL38 type PCFs, compared to the NL21 fibers, leads to these fibers being few-moded already at 1600 nm. Therefore, a scalar GNLSE simulation for this fiber did not reproduce many of the minor spectral structures, including the considerable share of energy propagated in the photonic lattice, despite including the wavelength dependence of the effective mode area. With this fiber, the fixed-A_{eff} simulation produced a spectrum with limited blue-shifted broadening, although this effect was not as much pronounced as in the case of the NL21C2 fiber. Notably, this occurs despite more curved dispersion profile of the NL38 series of fibers, compared to NL21 fibers, Fig. 3(b). Limited change of spectral width at the redshifted wavelengths in NL38A2 simulation is straightforwardly explained with reaching of the edge of glasses transmission window. In a lossless fiber scenario, the broadening in NL38 series fiber extends well beyond the verified transmission cutoff of the used glass. This is the evidence, which confirms that in these highly nonlinear fibers the location of the long-wavelength transmission edge is the limiting factor for SC bandwidth.

The nonlinear response of the fibers (γ – the nonlinear coefficient) is shaped by the effective mode area and the nonlinear refractive index, according the formula (neglecting for a moment its frequency dependence) $\gamma = n_2\omega_0/(c_0A_{eff})$, where n_2 is the nonlinear refractive index, ω_0 and A_{eff} are the angular frequency and the effective mode area of the pump wavelength and c_0 is the speed of light in vacuum. At the pump wavelength, the difference in the effective mode areas of the two types of fibers, Fig. 3(a), is roughly two-fold, with the NL21C2 fiber having an A_{eff} of 7.5 μm^2 and the NL38A2 of 15 μm^2. At the same time, the nonlinear refractive indices of the F2 glass and SF6 glasses differ by a factor of 7. However, n_2 can be reasonably safely assumed constant in the considered wavelength range, therefore the evolution of the nonlinear coefficient of the two discussed fiber series is primarily shaped

by the wavelength dependence of the effective mode area. The values of the nonlinear coefficient γ for both NL21C2 and NL38A2 fibers are summarized in Table 2. These values were calculated for the $A_{eff}(\lambda)$ profiles obtained numerically, shown in Fig. 3(a), and for fixed values of n_2.

Table 2. Values of nonlinear coefficient γ, nonlinear refractive index and effective mode areas for the NL21C2and NL38A2 fibers.

Fiber	1550 nm		2160 nm	
	A_{eff}	γ	A_{eff}	γ
NL21C2	$6.2\ \mu m^2$	$13.6\ W^{-1}km^{-1}$	$11.5\ \mu m^2$	$7.6\ W^{-1}km^{-1}$
	$n_2^* = 2.9 \times 10^{-20}\ m^2/W$			
NL38A2	$4.0\ \mu m^2$	$213.7\ W^{-1}km^{-1}$	$6.5\ \mu m^2$	$133.1\ W^{-1}km^{-1}$
	$n_2^{**} = 21 \times 10^{-20}\ m^2/W$			

* F2 glass, taken after [20], measured at 1240 nm
** SF6 glass, taken after [21], reported for 1500 nm

Over an order of magnitude difference in the fiber nonlinearity results in a situation, where the spectral broadening in the NL21 series fiber is mitigated by fiber attenuation at the long-wavelength edge of the pump laser spectrum, while in the NL38 series fibers the broadening continues up to the fundamental limit of the fiber's transmission window. The dynamics of the femtosecond-pumped ANDi SC is shaped by SPM and OWB and the latter is a degenerate parametric process which occurs at the instance of the temporal overlap of the interacting spectral components [10]. As a consequence of this, the shape of the ANDi fiber's dispersion profile, which determines the relative delays between the new arising SC wavelengths, can also be expected to influence the ANDi SC performance. Figure 3(b) shows that the NL38 series fibers feature less flat dispersion profiles than the NL21 series of fibers. Simulations presented in Fig. 6 for the scenarios of wavelength-independent and wavelength-dependent A_{eff} nevertheless confirm the dominating role of nonlinearity in efficient spectral broadening in this type of PCFs. Therefore the merit of the reported results stems from demonstrating a fiber design, in which a thermally matched pair of glasses of limited nonlinear response (NC21A/F2 in NL21 series) can be successfully substituted with a pair of commercially available glasses, of which the one used for the core has considerably higher nonlinear coefficient. Moreover, the resulting fiber has better mode confinement, which results in further nonlinearity improvement and coherent supercontinuum generation up to the glass infrared transmission cutoff.

5. Discussion

The emerging applications of broadband light sources increasingly often require excellent coherence properties of the delivered radiation. ANDi supercontinuum generation is a viable answer to this demand, and designing of efficient nonlinear ANDi fibers is a means to this end. In this work we highlighted the role of nonlinearity (nonlinear refractive index and wavelength dependence of the effective mode area) of ANDi microstructured fibers in formation of a coherent supercontinuum spectrum. We designed and fabricated two types of all-solid glass PCFs, using thermally matched glasses with different refractive index contrast. Both types of fibers had relatively broadband and flat normal dispersion characteristics, however they differed significantly in terms of the nonlinear response, owning to the different pairs of thermally matched glasses comprising their photonic lattices. In particular, one type of the discussed ANDi PCFs had the core area made of highly nonlinear SF6 glass, resulting in a factor of seven larger nonlinear coefficient than the previously reported all-solid oxide soft glass ANDi PCFs [15,17]. Since ANDi SC is driven by SPM from the onset of spectral broadening, the spectra recorded in this new type of fibers were the broader between the two discussed PCF types. In particular, the broadest spectrum was cutting off at 2750 nm, limited by the edge of transmission window of the silicate fiber glasses. The aim of this study was not to produce the flattest spectra but to investigate the role of the index contrast, nonlinearity,

attenuation and dispersion in coherent supercontinuum generation performance. Using numerical simulations based on a physically fabricated series of test fibers, we have shown that of these parameters, the fiber nonlinearity, in the context of both the nonlinear refractive index and the effective mode area evolution, play the major role in enhancing the obtainable supercontinuum bandwidth. Furthermore, these parameters outweighed the flatness of the ANDi dispersion profile, since as has been shown, the new PCFs with less flat dispersion but much higher nonlinearity (NL38 series) outperformed the less nonlinear but dispersion-flatter previous PCF design (NL21 series). Our results on the influence of the effective mode area on SC spectral width at the long-wavelength edge of the near-infrared are in agreement with results predicted earlier by Kibler et al. for anomalous dispersion-pumped fibers in [23]. Taking advantage of the possibility to design and fabricate ANDi PCFs using commercially available and relatively easy to handle silicate glasses (SF6 and F6 from Schott) facilitates the development of robust and broadband sources of coherent light. Preferably, such sources should utilize lasers operating at standard wavelengths, out of which the emerging thulium and thulium-holmium doped systems are particularly attractive. Applications of these devices can be easily found in e.g. two-tone spectroscopy, provided that the spectral reach extends across the near-infrared and over 3.0 µm. Silica and lead-silicate glasses are opaque at these wavelengths. Coherent supercontinuum in the mid-infrared can be obtained with chalcogenide fibers, albeit exotic pump wavelengths are required and these glasses do not transmit at wavelengths shorter than 1.0 µm [19,24]. Recently, modulation instability driven supercontinuum, based on cascaded silica, chalcogenide and fluorozirconate glass fibers has been demonstrated [25]. This concept could be adapted to the ANDi supercontinuum pumped with ultrafast thulium-doped fiber lasers. For this role, the demonstrated fiber labelled NL38A2 can be proposed. This is supported with its high nonlinearity, readily yielding spectral broadening up to the multiphonon absorption edge. A critical advantage of this fiber over e.g. a chalcogenide glass PCF is the potential to design its dispersion profile such that a standard wavelength pump laser can be efficiently used to initiate OWB already at this fiber. The consecutive fiber stage would then be expected to simply provide optimal group velocity matching and transmission for continuation of the OWB-based broadening, for which a chalcogenide PCF could be perfectly suited.

Funding